

Prediction of secondary flow losses in an entrance duct to a low-pressure turbine

P. JONAK¹⁾, T. BORZECKI²⁾, S. KUBACKI¹⁾

¹⁾ *Warsaw University of Technology, Faculty of Power and Aeronautical Engineering, Institute of Aeronautics and Applied Mechanics, Nowowiejska 24, 00-665 Warsaw, Poland, e-mail: pjonak@meil.pw.edu.pl*

²⁾ *Avio Aero, Grażyńskiego 141, 43-300 Bielsko-Biała, Poland e-mail: Tomasz.Borzecki@avioaero.it*

SECONDARY FLOW FEATURES AND TOTAL PRESSURE LOSSES by means of the total pressure loss coefficient are discussed in an entrance duct, named a turbine central frame (TCF), to a four-stage low-pressure turbine (LPT) of aero-engine. The mass-averaged total pressure losses are also analysed at outlets from selected components of the low-pressure turbine. The Reynolds-averaged Navier–Stokes (RANS) technique has been employed for prediction of mean flow characteristics. The numerical results are compared with experimental data obtained in Polonia Aero Lab in Zielonka (Poland). Good agreement is obtained between measured and predicted global flow characteristics and the pressure coefficient on a surface of an inlet guide vane. The high values of the loss coefficient are observed at endwalls, in cores of streamwise-oriented vortex structures near to the endwalls and in the wakes behind the vanes. It is found that the endwall losses contribute by far the most to the total losses at the outlets from the turbine central frame and first vane-row and they become lower at an outlet from the first blade-row and at outlets from consecutive vane- and blade-rows.

Key words: turbomachinery, low-pressure turbine, turbine central frame, secondary flow, Reynolds-averaged Navier–Stokes.

Copyright © 2019 by IPPT PAN, Warszawa

1. Introduction

AN EFFICIENCY OF THE LOW-PRESSURE TURBINE (LPT) strongly depends on a level of aerodynamic losses. The losses can be grouped into three parts: profile losses, tip leakage losses and endwall losses. The profile losses are determined by the flow over the blade or vane surfaces with a dominant contribution of the suction surface boundary layer. The tip leakage losses are caused by the flow through clearances at the tips of blades or vanes. The local imbalance between the pitch-wise pressure gradient and centrifugal force at endwalls, in a curvilinear motion of fluid elements through the vane-to-vane or blade-to-blade passages, results in a formation of the secondary flow motion. The losses associated with develop-

ment of the secondary flow motion are named the endwall losses. Although all three types of losses have their own origin, the total aerodynamic loss mechanism is complex as it involves multiple of mechanisms. Especially, an interaction between the endwall and the profile losses could be strong. We refer to the work by DUNHAM [1], SIEVERDING [2] and LANGSTON [3] for an extensive analysis of the secondary flow details in axial turbines. A recent review of secondary flow characteristics in turbomachinery applications is presented by LIGRANI *et al.* [4].

A nonuniform flow entering a cascade impacts the blade or vane leading edge. The boundary layer starts to roll up and forms streamwise-oriented vortices namely the pressure-side and suction-side legs of the horseshoe vortex. The suction-side leg of the horseshoe vortex develops near to the suction side of the blade. The pressure-side leg of the horseshoe vortex travels, due to a strong pitch-wise pressure gradient, towards the suction side of an adjacent blade. Downstream the cascade the pressure-side leg of the horseshoe vortex becomes a part of the passage vortex [2, 5]. The rotation senses of the pressure-side leg of the horseshoe vortex and the passage vortex are the same. The suction-side leg of the horseshoe vortex, rotating in an opposite sense to the passage vortex, might dissipate quite rapidly as it gets in contact with the passage vortex [2], might be entrained into the passage vortex [6] or eventually it may move along with the passage vortex [7].

Measurements of secondary flow details in a linear turbine rotor cascade at $Re = 2.9 \times 10^5$ (the Reynolds number based on the chord length and inlet velocity) was performed by ZUNINO *et al.* [8]. The thickness of the inlet boundary layer was equal to $\delta/h = 0.092$ (δ is a boundary layer thickness, h is a span). The hot-wire technique was used to obtain the velocity field and the Reynolds stresses distribution. GREGORY-SMITH *et al.* [9] used the hot-wire technique to investigate the secondary flow details in a linear turbine rotor cascade at $Re_2 = 5 \times 10^5$ (based on chord length and exit velocity). The passage and counter vortices were observed by means of the secondary velocity vectors and the total pressure contours at the outlet from the cascade. The cores of the total pressure losses were observed in the vicinity of elevated turbulent kinetic energy zones. But the location of the peak values of both quantities was not identical. An experimental study of flow through linear turbine cascade at $Re_2 = 4 \times 10^5$ was performed by GREGORY-SCHMIDT and CLEAK [10]. The thickness of the endwall boundary layer was equal to $\delta/h = 0.095$. Experimental study revealed a significant role of the normal Reynolds stresses in the total pressure loss production. The stereoscopic *PIV* technique was used in measurements of secondary flow features in linear cascade at $Re = 10^5$ by SANGSTON *et al.* [11]. The paths of the increased turbulent kinetic energy production were found to be well correlated with the paths of the total pressure losses along the blade passage. Modification of the profile shape near to the endwall resulted in a strong reduction of the total pressure

losses and the Reynolds stresses. A comprehensive study of the loss generation mechanism in turbomachines was made by DENTON [12]. The discussion of losses caused by viscous and turbulent mixing effects in the boundary layer flow, the heat transfer process, and shock waves was provided. HARRISON [13] reported the experimental study of flow through a linear turbine cascade. The endwall shear stress, measured by a hot film probe, was used to define the loss coefficient. Experimental results were compared with a simple aerodynamic model. Overall, good agreement was observed between the predictions using the aerodynamic model and reality. Some differences between the measured and predicted loss coefficient were only reported downstream the blade trailing edge. The differences were caused by neglect of the wake mixing losses in the model. The measurements of the leakage losses in the flow through the linear turbine cascade were performed by YAMAMOTO [14]. The measured total pressure losses proved to be strongly dependent on the clearance gap size and the flow angle. The formation of the leakage flow was observed mainly in the rear part of the tip. The interaction between the leakage flow vortices and the passage vortex was also reported. A two-part study, devoted to an empirical method development for prediction for secondary flow losses, was conducted by BENNER *et al.* [15, 16]. The new loss breakdown scheme with an improved correlation for the spanwise penetration depth of the passage vortex was reported in part I [15]. A novel empirical model for taking into account the secondary losses was presented in part II [16]. The comparison of predicted and measured cascade data was made on the considerably large database. It was found that a new secondary loss correlation requires a general scaling factor to give reasonable results for a wide range of flows.

ARISI *et al.* [17] performed a validation of three eddy-viscosity based and one second-moment closure numerical models against an experiment for flow and heat transfer modelling in a linear cascade with an endwall at $Re = 1.5 \times 10^6$. The second-moment closure model showed the best agreement with reality, among the models tested. An experimental and numerical study of the flow and heat transfer characteristics in the three-stage research turbine was made by SCHOBELI *et al.* [18]. The numerical results obtained with the $k-\omega$ *SST* model were in relatively good qualitative agreement with experiment. However, the overprediction of the heat transfer characteristics was observed. ZAMBONI and ADAMI [19] employed *RANS* and *URANS* techniques with the $k-\omega$ *SST* and explicit algebraic Reynolds stress (*EARSM*) $k-\omega$ models for analysis of the interaction between the leakage flow at the inner platform upstream of a single stage *HPT* blade and secondary overturning passage flow within the aerofoil. In general, quite good results were obtained for prediction of the total pressure at the rotor outlet using the steady *RANS*. The results were further improved employing the time-accurate *RANS*. Somewhat better accuracy was reported in capturing the three-dimensional flow features, with the *EARSM* than using the standard *SST*

model. STRAKA [20] studied the predictive capabilities of the $k-\omega$, *EARSM* $k-\omega$ and $k-\omega$ based hybrid *RANS/LES* models for simulation of unsteady flow through the low-power axial steam turbine. The numerical results were compared with their own experiment. All numerical results by [20] agreed quite well with measurements in terms of total-to-total efficiency at the outlet from the rotor. The differences between *RANS* and experiment were reported near to the peak values on the total-to-total efficiency profiles. The hybrid *RANS/LES* model provided improved results with respect to the *RANS*.

In the present work, the secondary flow structures and the total pressure losses are discussed for simulation of the flow through the four-stage low-pressure turbine (*LPT*) using the $k-\omega$ *SST* model. The simulation is performed without taking into account the flow leakage through clearances at the tips of blades and vanes. The discussion of the vortex structures nearby the shroud and hub in the entrance passage, called the turbine central frame (*TCF*) is provided. The analysis is preceded by an assessment of the three eddy-viscosity based models namely: the standard $k-\varepsilon$, the standard $k-\omega$ and the $k-\omega$ *SST* for simulation of secondary flow details near the endwall of the linear cascade by ZUNINO *et al.* [8]. First phase results were already presented at the conference [21]. The present contribution completes the study.

2. Computational details and turbulence model

In this section, a validation of three turbulence models is performed for simulation of flow through the 3D linear turbine cascade with endwall. The half-span single-blade cascade model was employed (Fig. 1). The numerical results were compared with experiments by ZUNINO *et al.* [8]. The Reynolds number based on the blade chord and inlet velocity was set to 2.9×10^5 . The inlet to the computational domain was placed at $0.6c_x$ (c_x is an axial blade chord) upstream of the blade leading edge. Profiles of two velocity components, turbulent kinetic energy and dissipation rate were imposed on inlet boundary according to experiment. Precursor *RANS* simulation of developing turbulent boundary layer flow was performed to reproduce the inlet profiles. The mean velocity components were projected onto the inlet plane of the cascade. The angle of attack (in the $x-y$ plane) was set to $= 41$ deg [8]. Good agreement is noted between measured and predicted inlet flow characteristics (results not shown). At the outlet, placed at $2c_x$, the static pressure was set to 1 atm. A symmetry boundary condition was applied at the midspan ($0.5h$, h is the span) located 150 mm from the endwall. The periodic conditions were imposed on side surfaces. The endwall and blade walls were treated as no-slip adiabatic walls.

The block-structured mesh with the boundary layer mesh near the blade surface was generated. At first, the surface mesh was defined at the endwall surface.

Next, the nodes were extruded in the spanwise z -direction. About 40 and 30 cells were employed inside the boundary layer on the blade surface and endwall, respectively. The computational grid consisted of about 7.2 million nodes. The maximum value of dimensionless wall distance $y^+ = u_\tau y / \nu$ (u_τ – friction velocity, y – distance to the nearest wall, ν – kinematic viscosity of fluid) was about 2 at all walls. The mesh coarsened by a factor of 2 with respect to the basic mesh was used for a grid convergence study. The differences in the predicted secondary flow details at the outlet from the ZUNINO *et al.* cascade between the basic and coarse meshes were small (not shown), so the basic mesh was considered for validation of RANS models.

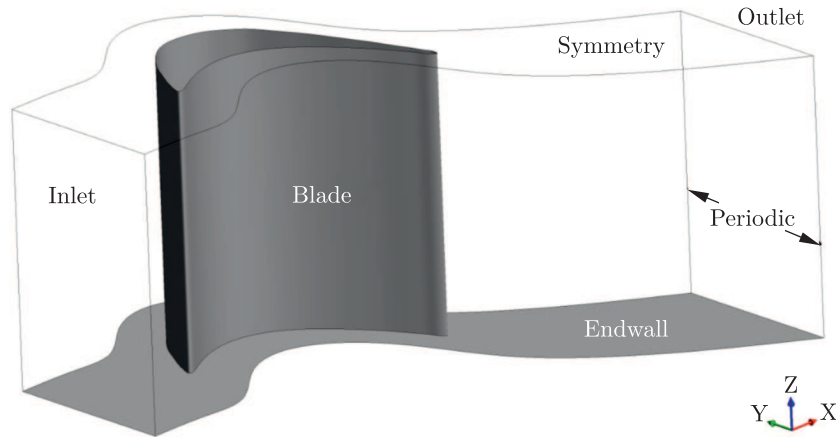


FIG. 1. Computational domain and boundary conditions for the linear cascade with endwall [8].

The steady flow simulation was performed. Air was treated as an ideal gas. The viscous work term was activated in the energy equation. A high resolution scheme of ANSYS CFX solver was applied for discretization of the momentum, continuity and transport equations. The scheme uses a non-linear algorithm for determination of the advection term coefficient at each node. The integration point data equal the upstream value plus a correction due to the gradient. The same numerical settings were used in the further analysis of flow through the four-stage *LPT* (Section 4). In flow simulation through the linear cascade the normalized solution residuals dropped below 10^{-4} and 10^{-3} with the $k-\omega$ and the $k-\varepsilon$ type models, respectively.

The scalable wall function was used in the simulation with the standard $k-\varepsilon$ model, whereas the automatic wall function was employed with the standard $k-\omega$ and $k-\omega$ *SST* models. In the wall function approach, the viscous sublayer region is bridged by empirical formulas with the turbulence dominated region. The

main idea of the scalable wall function is to replace the dimensionless distance from the wall in viscosity dominated region by the value at the intersection between the logarithmic and the linear profile. This way, the overprediction of the eddy-viscosity level is avoided near the viscous sublayer with the standard $k-\varepsilon$ model. In case of the $k-\omega$ -based models, a simple blending of the near-wall values of the turbulent quantities with their logarithmic layer counterparts is realized employing the automatic wall function technique.

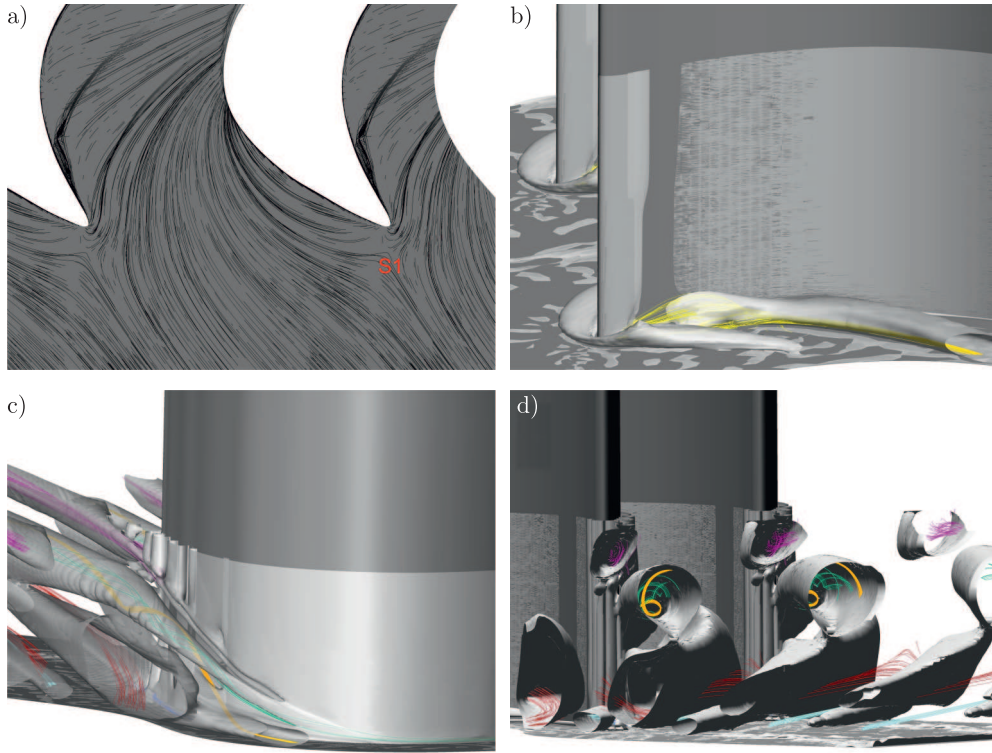


FIG. 2. Linear turbine cascade. Limiting streamlines at endwall (a) and vortex structures visualized by q -criterion near the leading edge (b), on the blade suction side (c) and at outlet from the cascade (d).

Validation of the turbulence models was made by comparing the numerical results with experiments at two streamwise distances, namely $x/c_x = 0.38$ and 1.19 (c_x – axial chord length). The cut at $x/c_x = 0.38$ was made as close as possible to the section called 'normal 4' in the experiment by ZUNINO *et al.* [8]. The comparison is made by means of the normalized turbulent kinetic energy:

$$(2.1) \quad q = \frac{2k}{U_1^2},$$

with k the turbulent kinetic energy and U_1 the mean velocity at midspan at the entrance to the cascade.

Figure 2a shows the streamlines along the endwall for the flow approaching the leading edge of the blade. The streamlines show the recirculation flow region in front of the blade, the saddle point (denoted by S1), and footprints of the pressure- and suction-side legs of the horseshoe vortex. Interestingly, the pressure-side leg of the horseshoe vortex is initially strongly pushed towards the pressure side of the blade (see yellow pathlines in Fig. 2b). Subsequently, it deflects from the pressure side of the blade, moves towards the suction side of the neighbouring blade and merges with the passage vortex. Figure 2c shows the secondary vortices on the suction side of the blade. The suction-side leg of the horseshoe vortex (depicted by green pathlines) is entrained into the passage vortex (orange pathlines). This is in agreement with the observation by SHARMA and BUTLER [6]. The current results show, that the suction-side corner vortex is formed at the streamwise distance about $x/c_x = 0.4$ (Fig. 2c). The suction-side corner vortex has the same sense of rotation as the passage vortex and it is generated at the intersection of the suction side of the blade and the endwall. Later on, this vortex merges with the passage vortex developing near to the blade surface, and very likely is responsible for shift of the passage vortex towards the mid-span downstream the cascade. The shift of the passage vortex was observed by ZUNINO *et al.* [8]. A formation of the suction-side corner vortex, rotating in the same sense as the passage vortex, was also reported in *LES* by BEAR *et al.* [22] and in *LES* and experiments by GROSS *et al.* [23] for the flow over a front-loaded L2F profile with endwall. In present work, the generation of the second vortex, rotating in the opposite sense to the passage vortex (counter vortex) is also reported near to the blade suction side (pink pathlines in Fig. 2c and d). A similar counter-vortex was also reported in measurements by WANG *et al.* [24] and recently by CUI *et al.* [25] and GROSS *et al.* [23]. GROSS *et al.* [23] emphasised that the separation of the suction-side boundary layer in the rear part of the blade at the height of the passage vortex was associated with development of the counter-vortex. Note that ZUNINO *et al.* [8] observed the three peak values of the normalized turbulent kinetic energy, q , near to the blade suction side in the rear part of the cascade (normals 7 and 8 in Fig. 6 in [8]): first very near to the endwall associated with the corner vortex, second at the height of the passage vortex and third related to separation of the passage vortex from the blade surface. ZUNINO *et al.* [8] were not able to measure the flow details very near to the blade surface due to technical reasons, thus the resulting counter-vortex was not detected in their measurements. But the flow separation under impact of the passage vortex was detected. Figures 2c and d show the formation of a broad corner vortex on the pressure side of the blade (red pathlines) and a tiny corner vortex (light blue) at the trailing edge on the

suction side of the blade. The evolution of the corner vortex was not mentioned in [8]. But one can see a large zone with negative values of the turbulent shear stress near to the blade pressure-side in Fig. 8e–g by ZUNINO *et al.* [8]. We suspect, that this might be associated with a development of the mentioned corner vortex. The small corner vortex on the suction-side of the blade was difficult to detect in measurements by ZUNINO *et al.* [8]. But the effect of this corner vortices was reported in [8] near to the endwall at streamwise distance $x/c_x = 1.19$ (see Fig. 9 of their paper). See also later Fig. 5a showing the contour plots of the measured turbulent kinetic energy at $x/c_x = 1.19$.

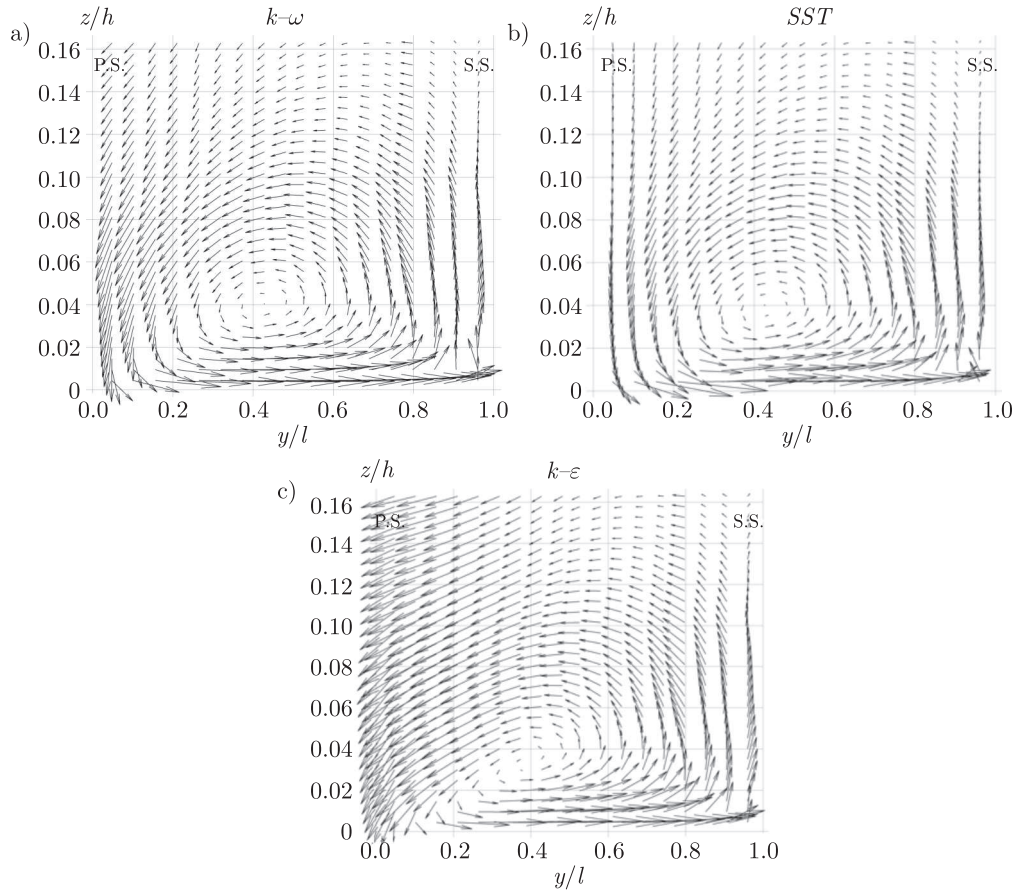


FIG. 3. Secondary flow vectors in y - z plane at a streamwise distance $x/c_x = 0.38$ obtained in simulations with different turbulence models.

Figure 3 shows the secondary velocity vectors at the streamwise distance $x/c_x = 0.38$, reproduced with the three models tested. Secondary velocity vectors are obtained by the difference between the time-averaged 3D flow field and

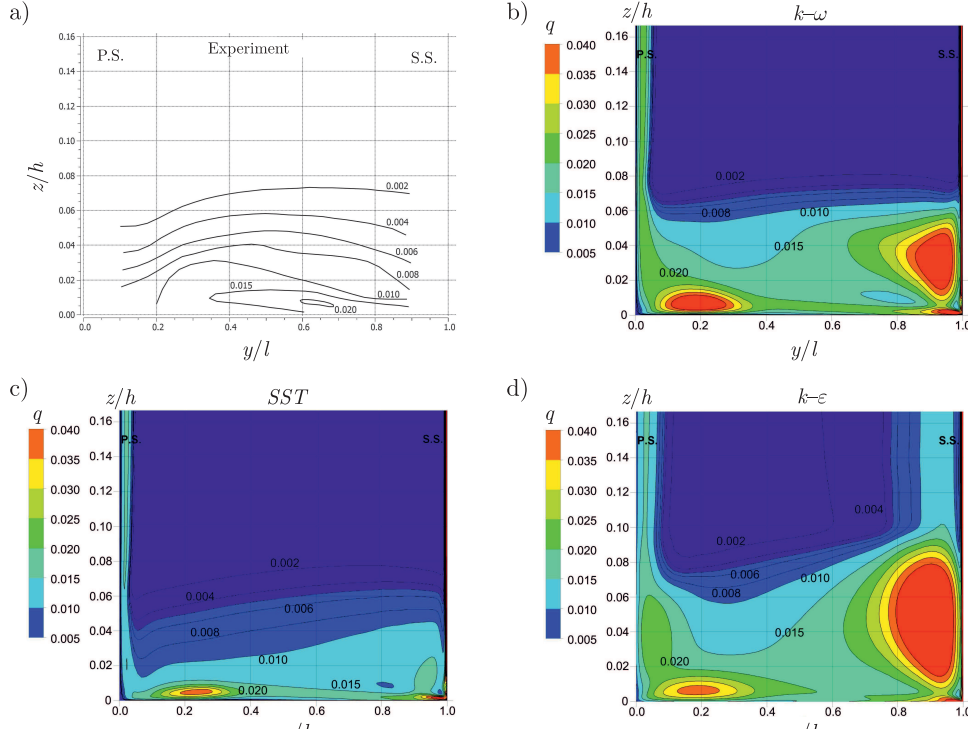


FIG. 4. Normalized turbulent kinetic energy in a y - z plane at a streamwise distance $x/c_x = 0.38$ obtained in measurement [8] (a) and in simulations (b)–(d).

a primary flow field, defined as the time-averaged flow at midspan. Good agreement is obtained between the measured (see Fig. 3d in [8]) and the predicted by the standard k - ω and the k - ω SST models the velocity vectors. The accuracy is much lower with the k - ϵ model.

Figure 4 shows the contour plots of normalized turbulent kinetic energy, q , in the y - z plane at $x/c_x = 0.38$ obtained in experiment by Zunino (Fig. 4a) and in simulation using the three turbulence models (Fig. 4b–d). The picture covers the distance between the pressure ($y/l = 0$) and suction ($y/l = 1$) sides of two adjacent blades and extends from $z/h = 0$ (endwall) up to $z/h = 0.16$ in the spanwise direction (vertical). Here, l denotes the distance between the pressure (P.S.) and suction (S.S.) sides of two adjacent blades in a y - z plane at $x/c_x = 0.38$. In measurements, the contours of q are not available in the immediate vicinity of blade surfaces, but they are well captured near to the endwall. The k - ϵ model (Fig. 4d) clearly reproduces a too high turbulent kinetic energy level near to the blade suction side and near to the right bottom corner ($y/l = 0.9$; $z/h = 0.04$). The turbulent kinetic energy level is much better reproduced in

this cross-section by the standard $k-\omega$ and $k-\omega$ *SST* models (Figs. 4b,c). None of the models reproduces a peak value of q nearby the endwall at $y/l = 0.65$ and $z/h = 0.01$ (Fig. 4a). Numerically, the peak value of q is reproduced at $y/l = 0.2$; $z/h = 0.01$ (Figs. 4b–d). Clearly, the *SST* model shows the best agreement with experiment, among the models tested.

Figure 5 presents the contour plots of the normalized turbulent kinetic energy, q , downstream the cascade ($x/c_x = 1.19$) obtained in experiment (Fig. 5a) and in simulations (Figs. 5b–d). The figure covers a single-pitch and the distance from $z/h = 0$ to 0.33 in the spanwise direction. Experiments show the three peaks of q : first near to the endwall at $y/p = 0.4$, $z/h = 0.02$, second at $y/p = 0.35$, $z/h = 0.12$ (35 mm) and third at $y/p = 0.55$, $z/h = 0.14$ (42 mm). The first maximal value of q is related to a development of the corner vortex on the blade suction side, the second is due to the passage vortex and the third is caused by interaction of the passage vortex with the blade boundary layer [8]. The current results show (see also Fig. 2c, d) that interaction of the passage vortex

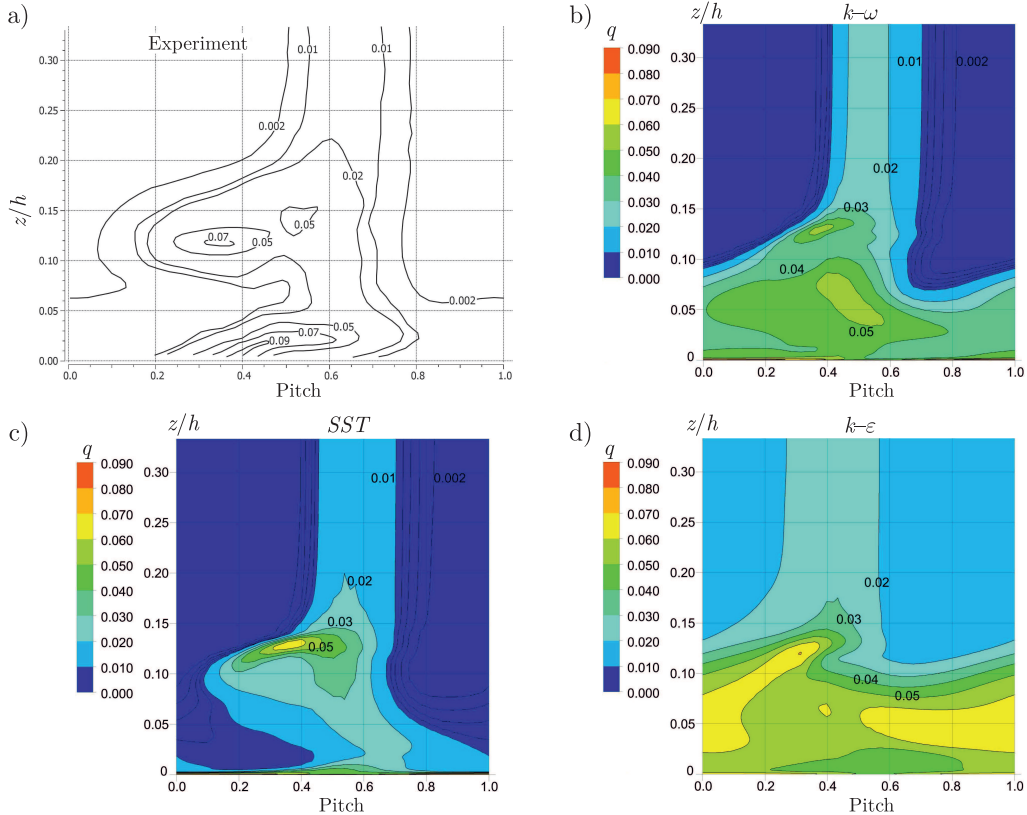


FIG. 5. Normalized turbulent kinetic energy in a y - z plane at a streamwise distance $x/c_x = 0.38$ obtained in measurement [8] (a) and in simulations (b)–(d).

with the blade boundary layer is accompanied by development of the counter-vortex. Table 1 summarises the measured and computed values of q , and their locations, at this downstream plane. The k - ε model completely fails in capturing the turbulent kinetic energy field at the outlet from the cascade. None of the models is able to reproduce the third peak at $y/p = 0.55$, $z/h = 0.14$ owing to a too strong dissipation of the counter-vortex. The 2D wake characteristics away from the endwall (for $z/h > 0.25$ in Fig. 5) also critically depend on the turbulence model. The centre of the wake (measured at distance $z/h = 0.33$) is located at $y/p = 0.62$, 0.50, 0.58 and 0.42 in experiments and predictions using the standard k - ω , SST and k - ε models, respectively (Table 1). The k - ω and the k - ε models show about 20% and 30% differences between the measured and predicted wake location. The best agreement is obtained with the SST model (6% difference). The SST and the standard k - ω models reproduce about 25–40% wider wake width with respect to experiment. The wake width is set to be equal to the pitchwise period y/p for which the q iso-lines drop to 0.01 level. The k - ε model returns much too high turbulent kinetic energy level in the 2D wake region, so it is not possible to estimate the wake width using the above criterion. Overall, the SST model gives the best agreement between simulation and experiment. The SST model is, therefore, selected for simulation of flow through the low-pressure turbine.

Table 1. Peak values of the turbulent kinetic energy and their locations ($y/p, z/p$) at a streamwise distance $x/c_x = 1.19$ for the Zunino cascade.

Case	Corner vortex on blade pressure side		Passage vortex		Counter vortex		2D wake centre location (y/p)
	Peak value	Location ($y/p, z/h$)	Peak value	Location ($y/p, z/h$)	Peak value	Location ($y/p, z/h$)	
Experiment	0.09	(0.4, 0.02)	0.07	(0.35, 0.12)	0.05	(0.55, 0.14)	0.62
k - ω	–	–	0.05	(0.38, 0.13)	0.05	(0.46, 0.06)	0.50
SST	0.05	(0.3, 0.01)	0.06	(0.38, 0.13)	–	–	0.58
k - ε	–	–	0.07	(0.31, 0.12)	–	–	0.42

3. Experimental rig

Measurements of main flow characteristics in the low-pressure turbine (LPT) were performed in Polonia Aero Lab in Zielonka (Poland). The LPT can be conceptually split into 11 parts: swirler, initial vane turbine central frame (TCF), four turbine stages (each consists of a set of vanes and blades) and exhaust vane turbine rear frame (TRF). The turbine central frame (TCF) is a duct connecting a high-pressure turbine with the low-pressure turbine. The flow leaving the high-

pressure turbine is, therefore, guided by the *TCF* vanes. Stationary elements in a front part of *LPT* are called swirler vanes and the inlet guide vanes. They guide the flow towards the first stage of *LPT*. Similarly, the stationary elements in every stage of the low-pressure turbine are also called vanes. The rotating elements are called blades. Later Fig. 7 gives the impression of the stationary and rotating elements of *LPT*. Figure 6 presents a schematic cross-section through the turbine axis and shows a location of traverse towers at an inlet to the *LPT* and at an outlet from the last stage. As shown in Fig. 6 the complete inner and outer surfaces are named a hub and a shroud, respectively. The global flow features (see discussion later) were measured in section 48 (after the main guide vane) and in section 55 (after the last stage of the *LPT*). Three traverse systems spaced 120° are situated at the inlet to the *LPT*. The five-hole probe that is installed in the traverse tower can rotate $\pm 15^\circ$ relative to its central axis (Fig. 6). The radial movement of the probe along the span enables measurement of the temperature and pressure field. The total cycle time for one traverse takes about 2 hours. The outlet of the *LPT* is equipped with the same test system. The measurements of the total pressure and total temperature field at inlet (Fig. 6) as well as the

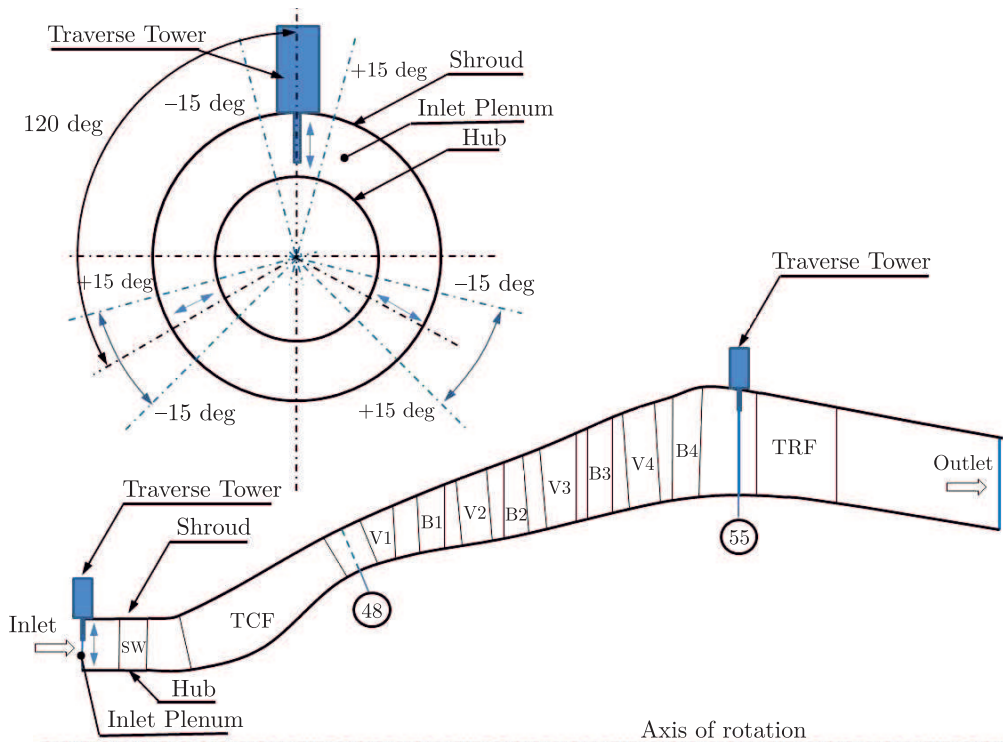


FIG. 6. Schematic of the LPT turbine. Cross-section through the turbine axis and visualization of traverse towers at the inlet to LPT and at the outlet from the last blade-row.

static pressure field at outlet allowed for calculation of area-averaged values of these quantities. The averaged values of the pressure and temperature were later imposed on inlets and outlets in numerical simulation (Section 4). The measurements of the static pressure on the surface of the inlet guide vane were also performed. The pressure distribution was measured by pressure taps placed at 20, 50 and 80% of the span. The mean distance between the taps is about 9% of axial chord length. The selected normalized pressure data is used for validation of numerical technique (see next section).

4. Flow through the four-stage low-pressure turbine

The rotating flow dynamics was taken into account using the Moving Reference Frame (*MRF*) method. This technique allowed to take into account the multiple rotating parts by activating the moving reference frame techniques in selected domains. As mentioned, the $k-\omega$ *SST* model with the automatic wall function technique was employed for prediction of the mean flow characteristics. Normalized solution residuals for all equations dropped below 10^{-4} in all cases discussed below.

4.1. Boundary conditions and interfaces

The inlet to the computational domain was placed at $2.6c_{x,SV}$ ($c_{x,SV}$ – axial chord of swirler vanes) upstream of the leading edges of the swirler vanes (Fig. 6). Constant values of total pressure and total temperature were imposed on the inlet to *LPT*, according to experiment (Section 3). The flow was assumed to be normal to the inlet plane. The turbulence intensity and turbulent to molecular viscosity ratio were set to the typical values: $Tu = 5\%$ and $\mu_t/\mu = 10$, respectively. The static pressure was defined at the outlet according to measurements. The surface normal gradients for all modelled scalars were set to zero at the outlet plane. The periodic boundary conditions were applied on side boundaries. Shroud, hub, vane and blade surfaces were treated as no-slip, adiabatic walls.

Two different approaches were considered for determination of fluxes of calculated variables at the interfaces between consecutive vane- and blade-rows. They are named the *Stage* and *Frozen Rotor* techniques according to ANSYS CFX. Only connection between the swirler and *TCF* domain, located in the front part of the turbine, was defined without the use of any interface technique. The pitch of the swirler domain was adjusted somewhat, in order to obtain 1 : 1 area contact between the swirler and *TCF* zone. The *Stage* technique is based on circumferential averaging of fluxes in bands at the outlet from a given part (domain). The averaged fluxes are later transmitted to the downstream part. The model is useful for large pitch ratios. Due to that, the *LPT* configuration

with single blade per each row downstream the *TCF* can be used. A preliminary analysis revealed that the mesh resolution in *TCF* region was of key importance for an accurate prediction of the global flow characteristics and the pressure distribution on the inlet guide vane surface. Therefore, the grid sensitivity study is only demonstrated for the *TCF* region (see discussion below). For that purpose, the *LPT* configuration with the *Stage* interface model is used. Note that with the *Stage* model the computational efforts are much lower than with the *Frozen Rotor* technique. Figure 7 gives the impression of the complexity of the computational domain using the *Stage* and *Frozen Rotor* techniques. An analysis of secondary flow details in the *TCF* region and determination of losses at outlets from every part of *LPT* is performed using the *Frozen Rotor* interface model. This technique produces a steady state solution to the local frame of reference on each side of the interface. The frame of reference and/or pitch is changed, but the relative orientation of the components across the interface is fixed. If the frame changes the appropriate equation transformations are made. If the pitch changes, the fluxes are scaled by the pitch change. Some of the vane and blade domains were multiplied to obtain the pitch change as close as possible to unity. This way the geometry scaling errors were eliminated. Employing the *Frozen Rotor* technique enables to track the swirler and *TCF* wakes downstream the *LPT*. This was crucial for analysis of the secondary flow details in the *TCF* region.

4.2. Grid sensitivity study

The flow simulation through the low-pressure turbine (*LPT*) was performed using a block-structured mesh. In order to generate a high-quality mesh, the computational domain of a single blade was divided into about 200 blocks. The vane and blade grids consisted of about 1 million nodes. The swirler, *TCF* and *TRF* meshes had about 1.3, 2 and 3 million nodes, respectively. Table 2 summarises the mesh details. The total number of nodes was equal to about 20 and 90 million using the *Stage* and *Frozen Rotor* interface techniques, respectively. The indexes of mesh quality measure for every part were verified to be within the allowable bounds (result not shown). 25 nodes and 1.15 growth ratio of a cell size inside the boundary layer in every part of the *LPT* were applied. The thickness of the boundary layer mesh zone (O-grid block) was estimated by correlation, by SCHLICHTING [26]

$$(4.1) \quad \delta = 0.37cRe_c^{-1/5},$$

where c denotes the chord and Re_c is the Reynolds number based on the chord and average inlet velocity to a given component of the *LPT*. For safety reason,

the size of the O-grid was defined to be about 20% larger than the boundary layer thickness given by the formula (4.1).

The three different density grids were generated in the *TCF* region for the grid-sensitivity study (cases 1,2 and 3 in Table 2). The number of nodes was set to 2, 4 and 8 million in the *TCF* region, respectively. The grid characteristics were not changed in other parts of the *LPT*. A great attention was paid to the grid resolution in the boundary layer region. About 25, 35 and 45 nodes inside the boundary layer zone for coarse, medium and fine grids in the *TCF* region were selected, respectively. The thickness of O-grid mesh and the growth ratio was kept the same in all cases. Figure 7 shows the contour plots of y^+ on surfaces of vanes and blades in the simulation using the *Stage* and the *Frozen Rotor* models with the fine grid in the *TCF* region. Hardly any difference between the results obtained using the *Stage* and *Frozen Rotor* models is observed. The maximal value of y^+ on the *TCF* vane surface did not exceed 6 and was less than 24 at other walls (surfaces of vanes and blades) in the simulation with the fine grid in the *TCF* region. The maximal values of y^+ on the surface of the inlet guide vane were equal to about 21 and 11 on coarse and medium meshes in the *TCF* region using the *Stage* model, respectively.

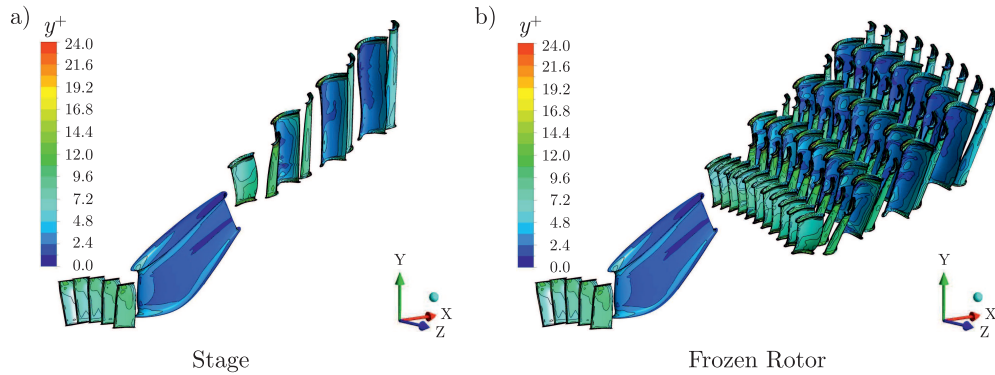


FIG. 7. Contour plots of y^+ on surfaces of vanes and blades in the simulation using the *Stage* (a) and *Frozen Rotor* (b) techniques.

Figure 8(a) shows an evolution of the pressure coefficient

$$(4.2) \quad C_p = \frac{p - p_1}{0.5\rho_1 U_1^2},$$

at 50% of the span on the *TCF* vane surface obtained on different density grids (simulations with the *Stage* model). In the formula (4.2) p , p_1 , ρ_1 and U_1 denote the mean static pressure on the blade surface and mean static pressure, density and the mean velocity at mid-span at the inlet to *LPT*, respectively. Hardly

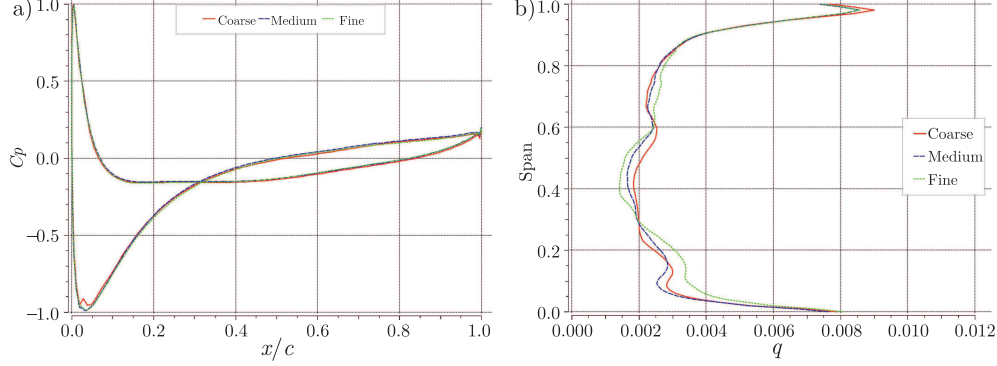


FIG. 8. Grid sensitivity study. a) pressure coefficient on TCF vane surface at 50% of span, b) profile of circumferentially averaged normalized turbulent kinetic energy at outlet from TCF in simulations using the Stage interface model.

any difference between the coarse, medium and fine grids is reported. Figure 8b shows the circumferentially averaged profiles of the normalized turbulent kinetic energy, q , at the outlet from *TCF*. Some differences are reported between 5 and 80% of the span. But the differences between the circumferentially averaged mean velocity and pressure profiles were very small (not shown). So one can conclude that a satisfactory level of agreement between medium and fine grids was obtained in the *TCF* region. The further analysis of the secondary vortex structures will be performed using the fine grid in the *TCF* region (simulation with the *Frozen Rotor* technique).

4.3. Comparison with experiment

Four simulations have been performed for a comparison of global flow features with experiments. The *Stage* interface model was used to connect the consecutive components of the *LPT* (except the swirler and *TCF* regions). As mentioned, the coarse, medium and fine meshes were used in the *TCF* region (denoted by cases 1,2 and 3 in Table 2). The fourth simulation was performed with the *Frozen Rotor* interface model on the fine grid in the *TCF* region.

Table 2 summarizes the relative difference (in percent) between measured and computed global flow characteristics, namely the mass flow rate (mf), total pressure (p_t) and total temperature (T_t), in sections 48 and 55 (see Fig. 6). The relative difference is expressed by

$$(4.3) \quad D = \frac{\varphi_{\text{num}} - \varphi_{\text{exp}}}{\varphi_{\text{exp}}} \times 100\%,$$

where φ_{num} and φ_{exp} are the numerical and experimental values of selected variables. An overprediction of the mass flow rate is not larger than 1.5% in

all cases analysed. The differences might be explained by the reduced losses due to the lack of the flow leakage through gaps at tips of blades/vanes in the present simulations. The very small differences are reported (about 0.4%) between measured and computed total mass-averaged pressures and total mass-averaged temperatures at sections 48 and 55.

Table 2. Relative differences (in percent) between measured and predicted global flow parameters of the low-pressure turbine and total number of nodes.

Case	TCF grid	Interface model	Total number of nodes (in millions)	Section 48			Section 55	
				mf [%]	p_t [%]	T_t [%]	p_t [%]	T_t [%]
Experiment	–	–	–	ref	ref	ref	ref	ref
Case 1	coarse	<i>Stage</i>	20.8	1.2431	–0.2173	0.2195	–0.2240	–0.2949
Case 2	medium	<i>Stage</i>	22.7	1.3812	–0.1284	0.2195	–0.2489	–0.3042
Case 3	fine	<i>Stage</i>	26.8	1.3352	–0.1581	0.2195	–0.2489	–0.2949
Case 4	fine	<i>Frozen Rotor</i>	98.7	1.4733	–0.1680	0.2170	–0.3733	–0.3840

Figure 9 shows distribution of the pressure coefficient on the TCF vane surface at 20% and 50% of span. The numerical results, obtained using the *Frozen Rotor* technique (Case 4 in Table 2), are compared with experiments. The measurement uncertainty of the pressure sensors is $\pm 0.05\%$. Some overprediction of C_p value at $x/c = 0.05$ can be observed. Somewhat too low C_p values are reported on both the suction- and pressure-sides of the vane between 40 and 70% of axial chord. But overall, a satisfactory level of agreement between the measured and predicted pressure coefficient on the TCF vane is achieved. One can conclude that the selected turbulence model is able to capture the main flow features and the pressure distribution on the inlet guide vane surface is in quite good agreement with reality.

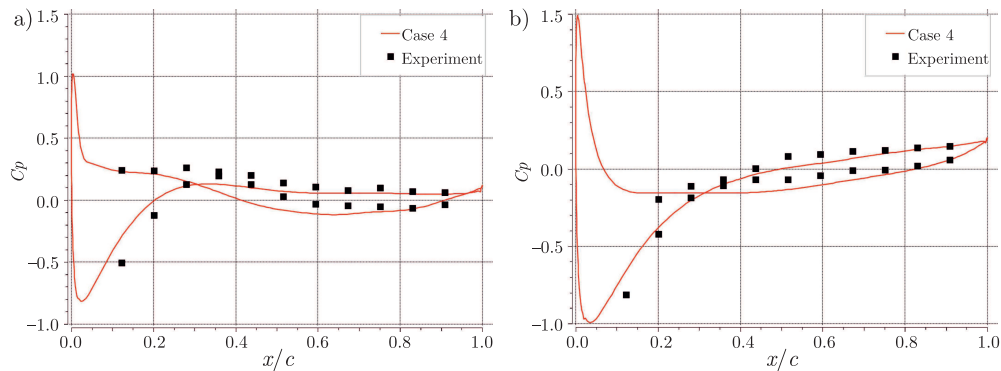


FIG. 9. Measured and predicted using RANS the pressure coefficient at 20% (a) and 50% (b) of the span on inlet guide vane surface.

4.4. Secondary flow details and losses

In this section, the secondary flow structures are analysed at endwalls of the swirler and inlet guide vanes. Next, the evolution of the total pressure loss coefficient is discussed at outlets from selected components of the low-pressure turbine.

Figure 10a shows the vortex structures, visualised by q -criterion (level 0.001), near to the shroud. The main flow is from the figure plane (as indicated by red arrow). The blue pathlines, released in the vicinity of the leading edges of swirler vanes are denoted by A–E symbols. The pathlines closely follow the streamwise-oriented vortex structures in the swirler domain. Symbols G and F (Fig. 10a) denote the pressure- and suction-side legs of the horseshoe vortex, developing around the inlet guide vane surface, respectively. An interaction of the streamwise-oriented vortex structures, originating from the swirler, with the pressure- and suction-side legs of the horseshoe vortex is reported. The two structures A and B interact with the suction-side leg (F) at the outlet from *TCF*.

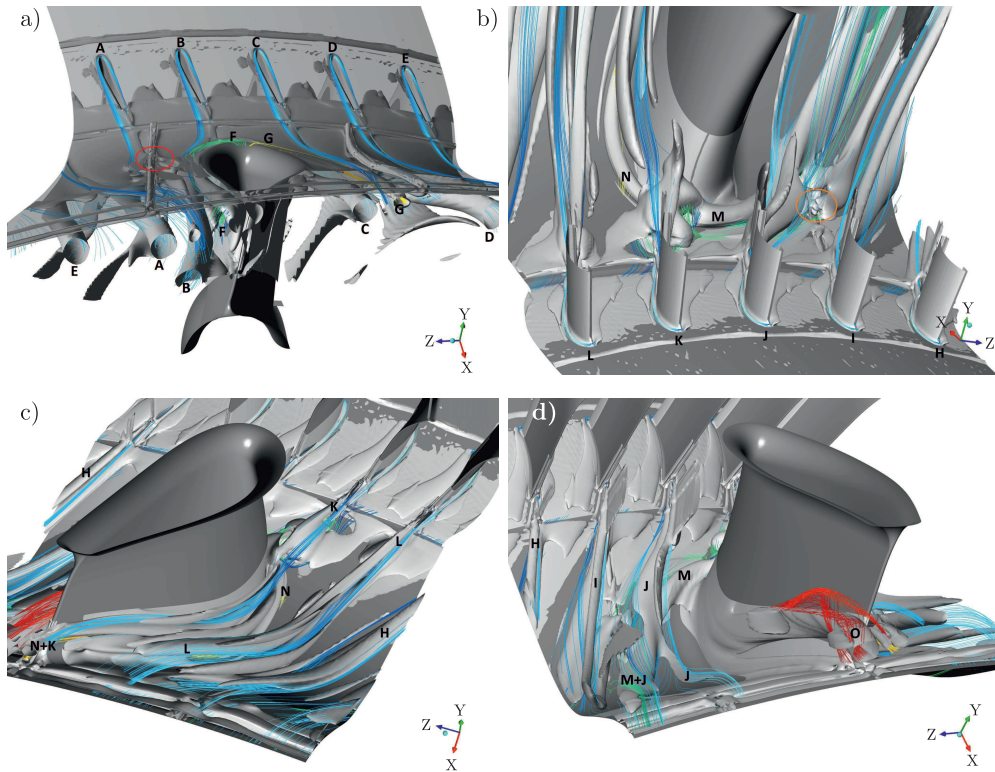


FIG. 10. Flow structures in swirler and TCF regions near to the shroud (a) and the hub (b)–(d). Panels (a), (c) and (d) show the view towards the turbine inlet. Panel (b) shows the view following the main flow.

A somewhat weaker interaction between another vortex, denoted by C symbol, and the pressure-side leg (G) can also be reported. Note that due to the technological and assembly reason, axially-oriented grooves are present on the shroud and hub in the *TCF* region. One can see an impact of A-vortex onto the axially-oriented groove. This impact is followed by a local flow separation (red circle in Fig. 10a). Figures 10b–10d show a development of the vortex structures near to the hub. In Fig. 10b the flow is towards the figure plane, whereas in Figs. 10c and 10d it is from the figure plane (see red arrows). In Fig. 10b the H–L symbols refer to the blue pathlines released in the vicinity of the leading edges of the swirler vanes at the hub. Similar as above, the streamwise-oriented vortex structures are formed at endwall in the vicinity of the swirler vanes. The approaching endwall boundary layer impacts and separates the inlet guide vane leading edge. Figure 10b presents a formation of the pressure- (symbol N) and suction-side (symbol M) legs of the horseshoe vortex near to the vane leading edge. An interaction of the vortex structure originating from the suction-side of one of the swirler vanes (K symbol) with the pressure-side leg of the horseshoe vortex (N symbol) is visible in Fig. 10c. Both vortices continue their development downstream and become visible at the outlet from *TCF* (N+K symbol). The suction-side leg of the horseshoe vortex (M symbol), unlike the pressure-side leg, is pushed away from the guide vane. Next, it gets in contact with the swirler wake denoted by J symbol. A perturbation of M and J vortices in the vicinity of one of the grooves can be observed. Again, the flow separation is noted there (depicted by an orange circle in Fig. 10b). The J and M vortices merge with each other and form a complex (M+J) structure at the outlet from *TCF* (Fig. 10d). A formation of a strong vortex structure, denoted by O symbol, is reported in the rear part of the *TCF* vane (Fig. 10d). The downstream development of this vortex structure is partly followed by red pathlines. The swirler wakes denoted by L and H symbols travel through the *TCF* passage without interaction with the inlet guide vane.

Next, an analysis of the total pressure loss coefficient is presented in the *TCF* region and at outlets from first and third vane rows. The total pressure coefficient is defined by:

$$(4.4) \quad Y_p = \frac{p_{t,\text{inlet}} - p_t}{p_{t,\text{inlet}} - p_{s,\text{outlet}}},$$

were $p_{t,\text{inlet}}$ is the mass-averaged total pressure at inlet to selected components of *LPT* (swirler, *TCF*, vane and blade rows). In formula (4.4) $p_{s,\text{outlet}}$ is the mass-averaged static pressure at the outlet and p_t is the total pressure. The total pressure at inlets and the static pressure at outlets are calculated in the middle part of surfaces, extending from 25% to 75% of the span. Figure 11 shows the contour plots of the total pressure loss coefficient in the *TCF* region at normalized streamwise distances $x/L_{TCF} = 0.1, 0.4, 0.6, 0.8$ and 1.0 (0.0 corresponds to an

inlet and 1.0 to an outlet from the *TCF* passage). The main flow is from the figure plane. The solid lines show the radial distances at 25% and 75% of span.

High values of losses are reported at endwalls and in the wakes shed by the preceding swirler vanes. The loss by the suction-side leg of the horseshoe vortex (F symbol) can be noticed in the vicinity of the fillet between the suction side of the *TCF* vane and the endwall (Fig. 11b). The grey circle shows the losses due to the flow separation under an impact of one of the vortex structures onto the axially-oriented groove. Further downstream, the increased losses are reported, nearby the fillet between the surfaces of the inlet guide vane and the shroud (Fig. 10d). They result from interaction of the suction-side leg of the horseshoe vortex (F symbol) with the endwall boundary layer. The loss associated with the pressure-side leg of the horseshoe vortex (G symbol) is visible very near to the shroud (Fig. 11b). Further downstream, the losses associated with interaction of the G-vortex and the C-vortex become clearly visible in Fig. 11c–11e.

The high value of loss is also reported near to the vane surface at the streamwise distance $x/L_{TCF} = 0.6$ (O symbol in Fig. 11c). It corresponds to a formation of the strong vortex structure in the rear part of the inlet guide vane. The interaction between B and O vortices (Fig. 11d and 11e) leads to intensification of the turbulent mixing. Figure 11e shows the total pressure loss coefficient at outlet from the *TCF* region. The oblique wake patterns originating from swirler vanes are still visible, but they become more tilted and spread in the cross-section with respect to the ones presented in Fig. 11a. High values of losses are observed behind the trailing edge of the *TCF* vane. The origin of these losses should be searched in a complex interaction between the streamwise-oriented vortex structures originating from the endwall boundary layers within the swirler passage (A and B symbols), the suction-side leg of the horseshoe vortex (F symbol) and the O-vortex.

One can notice a fairly large values of losses in the zone, denoted by K symbol, nearby the hub (Fig. 11a). This loss is associated with an impact of the K-vortex onto the leading edge of the guide vane. The losses associated with an interaction of this vortex with the pressure-side leg of the horseshoe vortex (N symbol) are visible in Fig. 11b–11e. Figure 11b shows an evolution of the total pressure loss coefficient at $x/L_{TCF} = 0.4$. As aforementioned, the wakes shed by the preceding swirler vanes become strongly tilted, as they pass through the *TCF* domain. The wake structure which is formed behind the middle swirler vane at the shroud (C symbol in Fig. 10a) travels towards the pressure side of the inlet guide vane (G symbol in Fig. 10a). The resulting losses are denoted by C and G symbols in Fig. 11b. At the same time, the wake structure which is formed behind the middle swirler vane at the hub (J symbol in Fig. 10d) moves over the suction side of the *TCF* vane. A quite large values of losses, denoted by M+J symbol, can be recognised in Fig. 11b–11e. They result from interaction of

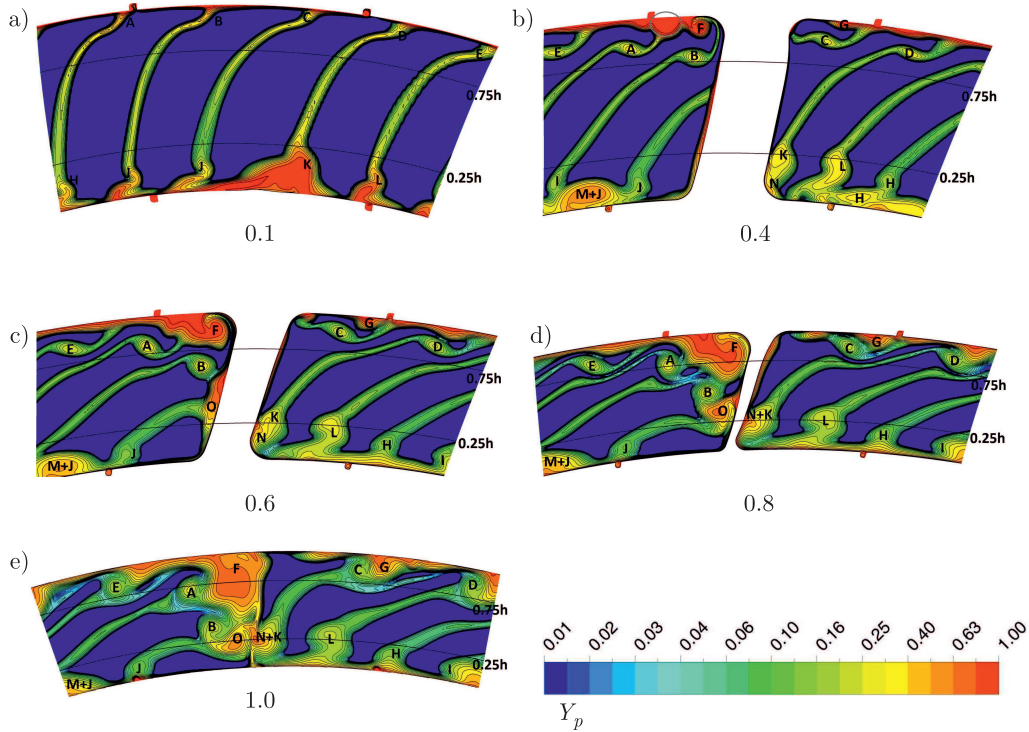


FIG. 11. Contour plots of the total pressure loss coefficient (Eq. (4.4)) at different normalized streamwise distances, (a) 0.1, (b) 0.4, (c) 0.6, (d) 0.8 and (e) 1.0 in TCF region.

the J-vortex with the suction-side leg of the horseshoe vortex (M symbol). The other zones of increased values of losses can also be recognized near to the hub (Fig. 11b–11e). They are caused by the streamwise-oriented vortex structures denoted by H, I and L symbols in Fig 11a. The high values of losses, resulting from interaction of these vortices with the endwall boundary layers, are clearly visible in Fig. 11b–11e.

Figure 12 shows the contour plots of the total pressure loss coefficient at the outlet from the first and third vane-row. High values of the losses are reported in the middle part of Fig. 12a, between fifth and third wakes from the right. They are due to turbulent mixing in the rear part of the preceding inlet guide vane (Fig. 10a). The increased losses are also reported in the wakes shed by the vanes and near to the hub and shroud. Note the high values of losses at endwalls which are associated with evolution of the streamwise-oriented vortex structures. Interestingly, the losses caused by the swirler wakes are also visible after the first vane-row (Fig. 12a). Further downstream (Fig. 12b), the losses in between the vane passages become more spread in the radial direction due to the centrifugal force in the preceding blade-rows.

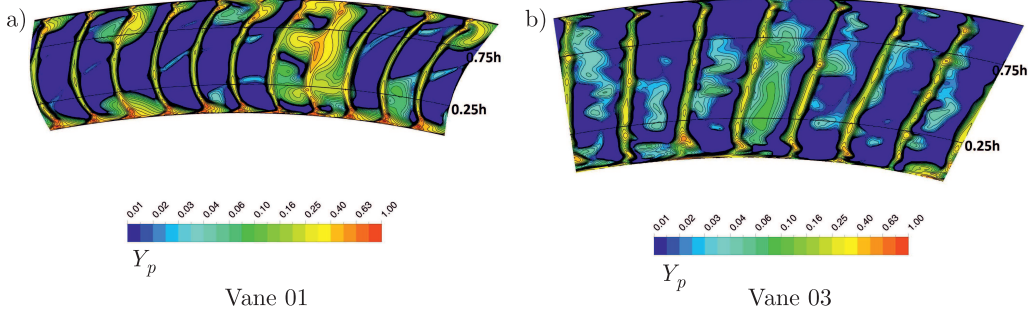


FIG. 12. Contour plots of the total pressure loss coefficient (Eq. (4.4)) at outlet from first vane-row (Vane 01) (a), and at outlet from third vane-row (Vane 03) (b).

Summing-up, the high values of the total pressure loss coefficient are observed at endwalls of the turbine central frame (TCF) and on surface of the inlet guide vane, in the cores of the streamwise-oriented vortex structures originating from the preceding swirler vanes, in the cores of the pressure- and suction-side legs of the horseshoe vortex formed around the inlet guide vane leading edge, and in the wakes behind the swirler and inlet guide vanes. At the outlet from the first vane-row, the high values of losses are observed in the endwall boundary layers, in the middle part of the cross-section by the turbulence mixing in the rear part of the preceding inlet guide vane and in the wakes shed by the vanes. Further downstream, most of the losses are associated with the endwall boundary layers and the turbulent mixing in the wakes behind the vanes and blades.

The further analysis of the losses within the TCF passage is presented in Fig. 13 by means of the mass-averaged total pressure loss coefficient

$$(4.5) \quad Y_p' = \frac{\int_A \rho U Y_p dA}{\dot{m}}.$$

The losses are analysed in the three regions: the endwall region near to the hub ($0.0h-0.25h$), the middle part ($0.25h-0.75h$) and the second endwall region near to the shroud ($0.75h-1.0h$). The mass-averaged total pressure loss coefficient calculated over the entire span ($0.0h-1.0h$) is also presented. The dashed vertical lines, denoted by LE and TE symbols, denote the leading and trailing edges of the guide vane. The mass-averaged total pressure loss coefficient increases downstream the passage. The figure shows that at the leading edge of the vane almost all of the mass-averaged losses are due to the secondary flow motion in the endwall regions ($0.0h-0.25h$ and $0.75h-1.0h$). Similar observation was made by CUI *et al.* [25] for LES study of flow through the linear cascade of T106A blades with and endwall (see Fig. 9b of their paper). At the outlet from the TCF region ($x/L_{TCF} = 1.0$) the contribution by the secondary vor-

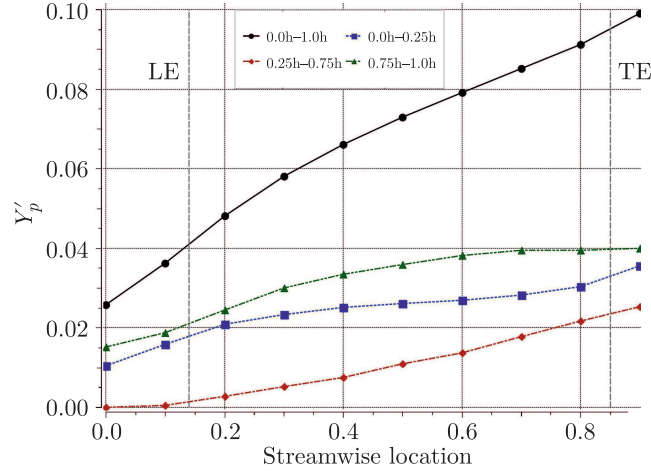


FIG. 13. Evolution of the mass-averaged total pressure loss coefficient (Eq. (4.5)) within the TCF passage.

tex structures near to the hub and the shroud becomes still very large (in total about 70%).

Table 3 summarises the percentage of the mass-averaged total pressure loss coefficient, given by Eq. (4.5), near to the hub ($0.0h-0.25h$), in the middle part of the section ($0.25h-0.75h$), and near to the shroud ($0.75h-1.0h$) at the outlet from *TCF*, and consecutive vane- and blade-rows. The secondary vortex structures near to the hub and shroud contribute by far the most to the mass-averaged total pressure losses after the *TCF* and first vane-row. As discussed, these losses are caused by strong streamwise-oriented vortex structures developing near to the hub and shroud in the *TCF* passage and the first vane-row. Further downstream, after the first blade-row, the profile loss ($0.25h-0.75h$) and the sum of losses at hub and shroud ($0.0h-0.25h$ and $0.75h-1.0h$) have a comparable contribution to the overall loss in the cross-section. The higher contribution by the profile losses is due to the larger aspect ratio of blades/vanes (see Fig. 6).

Table 3. Percentage of losses in three zones (0–25, 25–75 and 75–100% of span) at the outlet from selected components of low-pressure turbine. Symbols Vane01 and Blade01 denote the outlets from first vane-row and blade-row, respectively.

Span	<i>TCF</i>	Vane01	Blade01	Vane02	Blade02	Vane03	Blade03	Vane04	Blade04
0.00–0.25	31.01	39.47	25.23	38.05	24.91	31.43	24.51	45.15	24.26
0.25–0.75	28.42	29.21	51.72	45.41	50.54	60.43	51.56	52.34	49.22
0.75–1.00	40.57	31.32	23.05	16.54	24.55	8.14	23.93	2.51	26.52

5. Conclusions

The steady *RANS* technique has been employed for the prediction flow through the four-stage low-pressure turbine (*LPT*) of an aero-engine. Quite good agreement between the measured and predicted pressure coefficient on the inlet guide vane surface was reported. Good agreement between the measured and predicted global flow characteristics was obtained. The differences in the predicted global flow characteristics were less than 1.5%.

The secondary vortex structures within the swirler and inlet guide vane passages were analysed. The streamwise-oriented vortex structures, formed behind the inlet swirler vanes, influenced strongly the secondary flow characteristics in the endwall boundary layers within the guide vane and the first vane-row passages. The high value of the total pressure loss coefficient was reported in the close vicinity of endwalls. The secondary flow structures at the endwalls contributed by far the most (70–90%) to the overall mass-averaged total pressure losses in the inlet guide vane passage and at the outlet from the first vane-row. The profile losses were found to be dominant (about 50% of total) downstream the first blade-row.

Acknowledgements

The research work of the first author is partly supported by the Warsaw University of Technology statutory funds for young scientists in 2018. The second and third authors acknowledge a support from the research project COOPER-NIK financed partly by the Polish National Centre for Research and Development (INNOLOT/I/11/ NCBR/2014) and partly by Avio Polska Sp. z o.o. The work was also partly supported by the Interdisciplinary Centre for Mathematical and Computational Modelling (ICM) of the University of Warsaw (the grant ID GA73-24).

References

1. J. DUNHAM, *A review of cascade data on secondary losses in turbines*, Journal of Mechanical Engineering Science, **12**, 48–58, 1970.
2. C.H. SIEVERDING, *Recent progress in the understanding of basic aspects of secondary flows in turbine blade passages*, Journal of Engineering for Gas Turbines and Power, **107**, 248–257, 1985.
3. L.S. LANGSTON, *Secondary flows in axial turbines – a review*, Annals of the New York Academy of Sciences, **934**, 11–26, 2001.
4. P. LIGRANI, G. POTTS, A. FATEMI, *Endwall aerodynamic losses from turbine components within gas turbine engines*, Propulsion and Power Research, **6**, 1, 1–14, 2017.

5. L.S. LANGSTON, M.L. NICE, R. M. HOOPER, *Three-dimensional flow within a turbine blade passage*, Journal of Engineering for Power, **99**, 1, 21–28, 1977.
6. O.P. SHARMA, T.L. BUTLER, *Predictions of endwall losses and secondary flows in axial flow turbine cascades*, Journal of Turbomachinery, **109**, 229–236, 1987.
7. R.J. GOLDSTEIN, R.A. SPORES, *Turbulent transport on the endwall in the region between adjacent turbine blades*, Journal of Heat Transfer, **110**, 862–869, 1988.
8. P. ZUNINO, M. UBALDI, A. SATTÀ, *Measurements of secondary flows and turbulence in a turbine cascade passage*, ASME 1987 International Gas Turbine Conference and Exhibition, **1**, 1–9, 1987.
9. D.G. GREGORY-SMITH, J.A. WALSH, C.P. GRAVES, K.P. FULTON, *Turbulence measurements and secondary flows in a turbine rotor cascade*, Journal of Turbomachinery, **110**, 4, 479–485, 1988.
10. D.G. GREGORY-SMITH, J.G.E. CLEAK, *Secondary flow measurements in a turbine cascade with high inlet turbulence*, Gas Turbine and Aeroengine Congress and Exposition, 1990.
11. K. SANGSTON, J. LITTLE, M.E. LYALL, R. SONDERGAARD, *Effect of blade profile contouring on endwall flow structure in a high-lift low-pressure turbine cascade*, Journal of Turbomachinery, **139**, 21006–21011, 2017.
12. J.D. DENTON, *Loss mechanisms in turbomachines*, Journal of Turbomachinery, **115**, 4, 621–656, 1993.
13. S. HARRISON, *Secondary loss generation in a linear cascade of high-turning turbine blades*, Journal of Turbomachinery, **112**, 4, 618–624, 1990.
14. A. YAMAMOTO, *Endwall flow / loss mechanisms in a linear turbine cascade with blade tip clearance*, Journal of Turbomachinery, **111**, 3, 264–275, 1989.
15. M.W. BENNER, S.A. SJOLANDER, S. H. MOUSTAPHA, *An empirical prediction method for secondary losses in turbines — part I: A new loss breakdown scheme and penetration depth correlation*, Journal of Turbomachinery, **128**, 2, 273–280, 2005.
16. M.W. BENNER, S.A. SJOLANDER, S.H. MOUSTAPHA, *An empirical prediction method for secondary losses in turbines — Part II: A new secondary loss correlation*, Journal of Turbomachinery, **128**, 2, 281–291, 2005.
17. A. ARISI, D. MAYO, Z. LI, W.F. NG, H.K. MOON, L. ZHANG, *An experimental and numerical investigation of the effect of combustor-nozzle platform misalignment on endwall heat transfer at transonic high turbulence conditions*, Proceedings of ASME Turbo Expo, 2016.
18. M.T. SCHOBEIRI, K. LU, M. REZASOLTANI, *Effect of non-axisymmetric contouring on performance and film cooling of a rotating turbine endwall subjected to the secondary air purge: A combined numerical and experimental study*, Proceedings of the Institution of Mechanical Engineers, Part A: Journal of Power and Energy, **229**, 8, 813–831, 2015.
19. G. ZAMBONI, P. ADAMI, *On the unsteady interaction between the leakage and the main passage flow in a high pressure rig: CFD URANS investigations and comparison with the rig test data*, Proceedings of ASME Turbo Expo, 2016.
20. P. STRAKA, *Modelling of unsteady secondary vortices generated behind the radial gap of the axial turbine blade wheel*, VII European Congress on Computational Methods in Applied Sciences and Engineering, 2016.

21. P. JONAK, T. BORZECKI, M. KONOPA, S. KUBACKI, *Prediction of secondary flow features in a low pressure turbine*, Proceedings of ASME Turbo Expo, 2018.
22. P. BEAR, M. WOLFF, A. GROSS, C.R. MARKS, R. SONDERGAARD, *Experimental Investigation of total pressure loss development in a highly loaded low-pressure turbine cascade*, Journal of Turbomachinery, **140**, 3, 1–9, 2018.
23. A. GROSS, C.R. MARKS, R. SONDERGAARD, P.S. BEAR, J.M. WOLFF, *Experimental and numerical characterization of flow through highly loaded low-pressure turbine cascade*, Journal of Propulsion and Power, **34**, 27–39, 2018.
24. H.P. WANG, S.J. OLSON, R.J. GOLDSTEIN, E.R.G. ECKERT, *Flow visualization in a linear turbine cascade of high performance turbine blades*, Journal of Turbomachinery, **119**, 1, 1–8, 1997.
25. J. CUI, V.N. RAO, P.G. TUCKER, *Numerical investigation of secondary flows in a high-lift low pressure turbine*, International Journal of Heat and Fluid Flow, **63**, 149–157, 2017.
26. H. SCHLICHTING, *Boundary-Layer Theory*, 7th ed., McGraw Hill, New York, 1979.

Received August 10, 2018; revised version January 3, 2019.

Published online February 27, 2019.
